A new macroscopic strain hardening function based on microscale crystal plasticity and its application in polycrystal modeling

Sudeep Sahoo, Satyaveer Singh Dhinwal, Viet Vu, László S Tóth

A new macroscopic strain hardening function based on microscale crystal plasticity and its application in polycrystal modeling

Sudeep K. Sahoo[a,b,*], Satyaveer Singh Dhinwal[a,b], Viet Q. Vu[a,b,c], Laszlo S. Toth[a,b,d]

[a]Laboratoire d'Etude des Microstructures et de Mécanique des Matériaux (LEM3), CNRS UMR 7239, Université de Lorraine, 57045 Metz Cedex 1, France

[b]Laboratory of Excellence on Design of Alloy Metals for low-mAss Structures (DAMAS), Université de Lorraine, Metz, France

[c]Thai Nguyen University of Technology, Thai Nguyen, Vietnam

[d]University of Miskolc, Institute of Physical Metallurgy, Metal Forming and Nanotechnology, Miskolc, Hungary

Abstract

A new phenomenological strain hardening function is proposed to describe the strain hardening behavior of metallic materials. The function is based on a simplification of an earlier established self and latent hardening crystal plasticity approach. The proposed function contains only four parameters, which can be readily obtained using an efficient numerical technique by fitting the experimental curve. Several applications on different materials are presented and good agreements with the experimental counterparts were obtained. One great advantage of the proposed empirical function is that its parameters can be directly used in polycrystal viscoplastic modeling (VPSC approach) for crystal plasticity-based incremental strain hardening simulations. For the conversion of the parameters between the macroscopic scale and the grain-level, the Taylor factor was used, which was re-defined for polycrystals in the present work. The VPSC simulations also led to good reproduction of the experimental strain hardening behavior for all investigated cases, with rapid convergence.

Keywords: Strain hardening, Phenomenological function, Polycrystal plasticity, VPSC modeling

*Corresponding author: Sudeep K. Sahoo, sudeep.sahoo5511@gmail.com

1. Introduction

Strain hardening is considered to be one of the most important strengthening mechanisms as it plays a critical role in evaluating the material's functional properties and determines its suitability for engineering/structural applications. In general, such a characteristic response is obtained experimentally from the macroscopic response of a specimen loaded under simple compression, tension, or shear in the form of a stress-strain curve. Depending on material properties (such as crystal structure, grain size, etc.) and imposed loading conditions, the shape of a stress-strain curve varies significantly and frequently shows distinct stages [1-8]. In this aspect, finding a suitable empirical function that can reproduce the experimental measurements is a challenging task and has been the subject of numerous investigations. Indeed, analytical functions are useful in assessing material performance for design purposes.

Under this premise, well-known and widely used classical constitutive relations either follow a power-law or an exponential form. Examples for the former were suggested by Ludwik [9], Hollomon [10], and Swift [11], while the Voce-approach [12] was proposed for the latter. The drawback of the mentioned power-law form approaches is that there is no upper limit for the flow stress, while a final saturation stage of strain hardening is frequently observed, especially during severe plastic deformation [3]. To account for the saturation stress, the exponential form of the Voce-equation [12] has received special attention in which the flow stress approaches an asymptotic value at a high strain level. Subsequently, several approaches were proposed in this context that used an increased number of fitting parameters to capture the stress-strain response [1,13]. Chinh et al. [3] introduced an exponential power-law constitutive relationship that reduces to the conventional Hollomon power-law relationship at low strains and to the Voce exponential relationship at high strains. They demonstrated that the approach was effective in capturing the stress-strain relationship of high purity aluminum and copper over a wide range of strain, however, non-negligible deviations still existed in their findings for high strains. Recently, Lavakumar et al. [7] presented an improved empirical version of the Ludwigson [1] equation with additional terms and fitted parameters and applied successfully to several materials. Other approaches were based on the physical deformation mechanisms observed at the dislocation scale, for example, the Kocks-Mecking approach, which is very suitable for Stage III hardening [14-16] and the dislocation cell-based theory of Estrin et al. [2] to reproduce Stages III and IV.

Besides, the fit of an experimental stress-strain curve is also possible by crystal plasticity-based approaches where the parameters refer to strain hardening of individual slip systems, capable of distinguishing self and latent hardening [17-20] using a power-law relation with a saturation stress. Such physically-based approaches have proven to be effective for many materials and are well suited for a wide variety of loading conditions as well as deformation to large strain regimes (for example: Zhou et al. [19]; Wu et al. [21]; Dhinwal and Toth [22]; Sahoo et al [23]; Vu et al. [24]). Nevertheless, one of the challenges of such approaches is to determine the optimal values of the crystal plasticity-based strain hardening parameters. In this regard, various experimental [25-27] and computational [28-31] optimization methodologies were suggested to identify an optimal set of material hardening parameters for crystal plasticity models. The most conventional approach for identifying crystal plasticity hardening parameters is to carry out simple mechanical tests on a single crystal [25,26]. However, this is seldom practiced as most of the materials are often available as polycrystals, and the boundary conditions are very different for a crystal embedded into the polycrystal. A usual way is to use the inverse analysis technique which involves calibrating the material parameters until the simulation results match the experimental data. This is primarily based on the least-square method or simply using a trial-and-error approach. The former refers to an optimization process where a set of parameters is recognized for an objective function that minimizes the variance between the experimental data and the computed response. While the latter corresponds to a manual searching of each parameter by iteratively fitting the experimental curve. However, both of these approaches require initial estimation of the parameter values and involve a large number of iterations in an effort to converge to an optimal solution. At the same time, such techniques reflect two key sources of ambiguity for the quantitative estimation of parameters: (i) *uncertainty,* which occurs because of the presence of numerous associated unknown parameters within the phenomenological constitutive law, such that the effect of one parameter can be compensated by the other set of parameters on the course of strain hardening, and (ii) *inconsistency,* because the obtained values of the parameters are arbitrary. Consequently, to validate the experimental findings, these techniques are very complex and usually it is difficult to interpret the physical meaning of the parameters.

Therefore, to exploit the full predictive potential of the adjustable hardening parameters in a single expression, it is necessary to establish a meaningful and optimized set of hardening parameter values. With the advancement in computational technology, several

researchers have proposed inverse analysis strategies for the computational optimization algorithm by employing sophisticated experimental techniques [32-39]. The experimental results can be achieved by the most commonly available instrumented techniques such as nano-indentation or digital image correlation (DIC). The former involves probing individual grains within the polycrystal and extracting the indentation stress-strain response in the form of the load-displacement curve for several grains within the polycrystal, which is then used to construct the macroscopic response [32-37]. In this regard, Patel et al. [35] utilized spherical indentation to establish a correlation between the indentation stress-strain curve and the uniaxial stress-strain curve via simple scaling factors. Subsequently, they validated these scaling factors using a finite element (FE) model. Mandal et al. [36] established a canonical correlation analysis to explain the influence of the constitutive model parameters on the flow stress behavior within the framework of the mechanical threshold stress (MTS) model [40]. However, owing to the complex stress state beneath the indenter, it is difficult to interpret the experimental results and obtain the parameters that govern the hardening behavior. Also, these experimental strategies are very time-consuming as the number of experiments to be carried out on several grains is large, and incurs a huge experimental cost, with an additional drawback of the indentation size-effect.

Alternatively, within the framework of experimental techniques, DIC enables the measurement of spatial displacement and strain fields and provides an insight into the micromechanics of solids. Guery et al. [38] used the inverse analysis technique for coupling the experimentally measured spatial strain fields produced via DIC and the weighted finite element modeling update (FEMU) scheme for qualitative estimation of the crystal plasticity parameters. The FEMU approach is based on comparing the results of FE modeling with experimental results, by minimizing the error. However, to converge into an acceptable solution, the method requires numerous FEM calculations. Despite these advancements, a time-efficient methodology is always sought which could overcome the computational cost and at the same time provide an approximation to the values of the uncertain parameters present in the strain hardening functions.

Based on this perspective, the present investigation is undertaken with two major objectives: (i) A new analytical version of the strain hardening function based on a power-law relation is proposed, which has its origins in crystal plasticity. Unlike all other existing empirical power-law functions, this power-law function is unique in the sense that it has saturation stress that can drive the flow stress to saturation. (ii) A suitable minimization

technique is proposed for determining the optimal values of the unknown hardening constants. The reliability of the proposed approach was tested critically by applying it to different materials: Aluminum, Copper, Steel, and Titanium, undergoing various deformation modes, such as tensile, compression, as well as torsion testing, and demonstrated good fitted response. To this end, the parametric values obtained from the proposed procedure were also employed in a crystal plasticity framework, which includes much more physics on the deformation of the polycrystal than a phenomenological function. The VPSC (viscoplastic self-consistent) polycrystal model was used for this purpose, and the obtained strain hardening was also in good agreement with the experiments, like the phenomenological one. The great advantage of doing first a phenomenological fitting before the VPSC simulation is that the phenomenological parameters serve as an excellent initial guess for the crystal plasticity simulations. In this way, the VPSC simulation work is highly reduced, and the obtained results are remarkable.

2. The principles of the new strain hardening function

In crystal plasticity, strain hardening is frequently modeled using self and latent hardening of the slip systems. One of the frequently used approach was introduced by Kalidindi et al. [18], then later modified by Zhou et al. [19]. It expresses the influence of all slip systems on the hardening rate of a given slip system '*i*' and is given by:

$$\dot{\tau}_0^i = \sum_{j=1}^{n} q_c^{ij} h_c \left(1 - \frac{\tau_0^j}{\tau_{sat}^j}\right)^{a_c} \left|\dot{\gamma}^j\right|. \tag{1}$$

Here, τ_0^i is the resolved shear stress in slip system *i*, $\dot{\gamma}^j$ is the resolved shear strain rate in the slip system *j*, and *n* is the total number of slip systems. q_c^{ij} denotes a (*n* x *n*) matrix and accounts for the self and latent interactions between the slip systems (the index '*c*' stands for 'crystal plasticity'). The diagonal elements of q_c^{ij} represent the effect of self-hardening, while the off-diagonal parts are the latent hardening terms [17]. h_c and a_c are the hardening parameters, and τ_{sat}^i denotes the saturation stress. The essential novelty of the present work is to use an analytical version of this hardening rule, applicable at the macroscopic level:

$$\dot{\sigma}_0(\bar{\varepsilon}) = h\left(1 - \frac{\sigma_0(\bar{\varepsilon})}{\sigma_{sat}}\right)^a \dot{\bar{\varepsilon}}\,. \tag{2}$$

Here $\dot{\bar{\varepsilon}}$ is the macroscopic von-Mises equivalent strain rate and σ_0 is the reference strength of the material, which appears in the strain rate sensitive power-law formula of viscoplastic behavior:

$$\sigma(\bar{\varepsilon}) = \sigma_0(\bar{\varepsilon})\left(\frac{\dot{\bar{\varepsilon}}}{\dot{\bar{\varepsilon}}_0}\right)^m, \tag{3}$$

with *m* being the macroscopic strain rate sensitivity index and $\dot{\bar{\varepsilon}}_0$ the reference strain rate.

It should be noted here that in the above formulation, the self and latent hardening have been simplified and thus, do not appear in the formula. Also, while there can be several different values for τ_{sat}^i in Eq. (1), the macroscopic curve can contain only one parameter for the saturation stress; σ_{sat}. After separating the variables and integrating Eq. (2), the following form of the strain hardening function can be obtained:

$$\sigma_0(\bar{\varepsilon}) = \sigma_{sat} - \sigma_{sat}\left[\left(\frac{h(a-1)}{\sigma_{sat}}\right)\bar{\varepsilon} + \left(1 - \frac{\sigma_{00}}{\sigma_{sat}}\right)^{1-a}\right]^{\frac{1}{1-a}}, \text{where } a \neq 1. \tag{4}$$

Here σ_{00} is the yield strength of the material (at $\bar{\varepsilon} = 0$). The number of unknown parameters in this function is four; they are: σ_{00}, σ_{sat}, *h*, and *a*. Among these, σ_{00} can be readily assigned from the experiment. While the values of the remaining three parameters (i.e., σ_{sat}, *h*, and *a*) cannot be assigned directly; they need to be identified from the experimental curve using a suitable fitting procedure. A relatively simple and fast procedure is a minimization technique, which is presented in the next section.

3. Parameter identification procedure

The first parameter is the yield stress (σ_{00}), thus the flow stress value at the beginning of the plastic strain (ε = 0). To obtain the other three parameters, a large number of

co-ordinate points were selected on the experimental flow stress curve; typically, about N=50, and the following scalar function was defined:

$$f = \sum_{i=1}^{N} \left| \sigma_i^{sim}(\bar{\varepsilon}_i) - \sigma_i^{\exp}(\bar{\varepsilon}_i) \right| = \min. \tag{5}$$

Here the superscripts '*sim*' and '*exp*' stand for the stress value from Eq. (4), and the experimental one, respectively. An efficient procedure for minimizing this function is to employ a suitable bracketing technique until the function's value (f) approaches zero with the specified precision. To begin the bracketing process, large initial intervals were defined for each of the three parameters. In the current study, the intervals of the parameters were: $\sigma_{sat} \in [\sigma_{00}, 1000 \text{ MPa}]$, $h \in [0, 100000 \text{ MPa}]$, and $a \in [1, 10, a \neq 1]$. At the very beginning, each of these intervals were divided into 100 equal intervals and the function values f were calculated for all possible combinations of the 100^3 parameter values, then the parameter combination corresponding to the minimum f value was identified. Subsequently, in the next iteration, the same procedure was repeated on the reduced intervals (which were divided into 100 intervals), and the cycle continued several times, until the minimum f value reached the required precision (0.01 MPa). The mentioned procedure is computationally very fast, it converges in seconds to achieve the specified precision [see the Fortran program as an additional available material at *LaszloSToth/Hard-fit-by-minimization: An efficient Fortran program to fit a stress-strain curve by the empirical function derived from crystal plasticity. (github.com)*].

For the special case, when $a = 1$, we obtain from Eq. (2):

$$\sigma_0(\bar{\varepsilon}) = \sigma_{00} + h' \cdot \bar{\varepsilon} \ , \text{ where } \ h' = h \cdot \left(1 - \frac{\sigma_{00}}{\sigma_{sat}} \right) \ . \tag{6}$$

So, for $a = 1$, the strain hardening is linear. Therefore, for linear hardening, the meaning of the σ_{sat} parameter is not a saturation stress, it is just a parameter with stress dimension. In this case, only one point is needed from the experimental curve to obtain the value of the h' parameter (if σ_{00} can be read from the experimental curve).

The proposed new function in Eq. (2) can only describe hardening, because the term $\left(1-\frac{\sigma_0(\bar{\varepsilon})}{\sigma_{sat}}\right)$ must be positive. Softening corresponds to $\sigma_{sat} \le \sigma_0(\bar{\varepsilon})$. In this case, the integration of Eq. (2) leads to the following:

$$\sigma_0(\bar{\varepsilon}) = \sigma_{sat} + \sigma_{sat}\left[\left(\frac{h(a-1)}{\sigma_{sat}}\right)\bar{\varepsilon} + \left(\frac{\sigma_{00}}{\sigma_{sat}} - 1\right)^{1-a}\right]^{\frac{1}{1-a}}, \quad \text{(for softening: } \sigma_{sat} \le \sigma_{00}\text{)}. \qquad (7)$$

4. Use of the macroscopic hardening parameters in polycrystal plasticity simulations

One of the main goals of the proposed methodology is to evaluate and assess the identified hardening parameters so that they can be conveniently used in crystal plasticity simulations. Indeed, it is a challenging task to perform a high-quality numerical work for simulating the macroscopic strain-hardening behavior of polycrystals with crystal plasticity approach. Nevertheless, it is often successful, as there are excellent simulation results published in several studies [22-24, 41-45]. The usual technique used is trial and error, which requires many iterations. However, when there are initial parameters that are already good approximations, the task becomes much more efficient. Indeed, as the proposed macroscopic strain hardening function was obtained by simplifying a microscopic (crystal plasticity) modeling function, it is possible to use the macroscopic parameters as a good initial guess for the crystal plasticity simulations.

There are differences between the values of the macroscopic and microscopic hardening parameters which are due to the difference in the scale of the mechanical behavior. Therefore, one has to link the two scales. One possibility is to use the Taylor factor which relates stress and strain between the two scales. The Taylor factor is based on the energy balance between the grains (‘internal energy’) and the macroscopic sample (‘external energy’). For linking the microscopic and macroscopic properties, the polycrystal has to be considered as a composite material. Therefore, the Taylor factor has to be based on an energy relation that is established for composites. In all previous works, the Taylor factors used for polycrystals were based on the equality of the external and ‘the apparent internal energies’ (see its definition in the Appendix), which is valid only in two cases: iso-stress and iso-strain, or also called Static and Taylor approaches. In other approaches (like the widely used Self-

232 Consistent model), the external and the 'apparent internal energies' are not equal, so a
233 correction is needed. Moreover, there are actually two kinds of Taylor factors; one used for
234 the strains (equivalent strain macroscopically and crystallographic resolved shear strain
235 within the grains) and another which is relating the stresses between the two scales
236 (equivalent stress at the macroscopic level, and crystallographic resolved shear stress in the
237 grains). The definitions of the two kinds of Taylor factors were established in the Appendix
238 in such a way that the energy balance for polycrystals is correctly used.

239 We recall first the resulting definition relating the strain quantities:

240 $$M(\text{for strain}) = \frac{\sum_{g=1}^{n_g}\sum_{f=1}^{n_f}\sum_{s=1}^{n_s}\left(\left|\dot{\gamma}_s^f\right|\cdot v_g\right)}{\bar{\dot{\varepsilon}}_c} \ , \qquad (8)$$

241 Here $\dot{\gamma}_s^f$ is the slip rate in the slip system identified with the index '*s*' for the slip-family '*f*'
242 (if there is more than one slip system family; frequent in b.c.c. and h.c.p. crystal structures),
243 whereas, n_f is the number of slip families, and n_s is the number of slip system in a slip
244 family. n_g is the number of grains and v_g is the relative volume fraction of the grain (so that
245 the total volume is 1.0). The Taylor factor for converting the stress quantities at the two
246 scales is:

247 $$M^{(\text{stress})} = \frac{\bar{\sigma}_c}{\lambda\cdot\bar{\tau}_r} \ , \qquad (9)$$

248 where $\bar{\sigma}_c$ is the macroscopic equivalent stress and $\bar{\tau}_r$ is the average resolved shear stress in
249 the slip systems (see its definition in the Appendix). The λ parameter expresses the ratio of
250 the 'external energy' to the total 'apparent internal energy' of the individual grains:

251 $$\lambda = \frac{\underline{\underline{\sigma}}_c : \underline{\underline{\dot{\varepsilon}}}_c}{\sum_{g=1}^{n_g} \underline{\underline{\bar{\sigma}}}_g : \underline{\underline{\bar{\dot{\varepsilon}}}}_g \cdot v_g} \ . \qquad (10)$$

252 Here $\underline{\underline{\sigma}}_c$ and $\underline{\underline{\dot{\varepsilon}}}_c$ are the stress and strain rate tensor at the macroscopic level, $\underline{\underline{\sigma}}_g$, $\underline{\underline{\dot{\varepsilon}}}_g$ are the
253 same at grain level. (Note that λ is <u>*not*</u> equal to 1.0 in composite materials, see in Ref. [46].)

254 The Taylor factor for converting the strain quantities at the two scales is:

$$M^{(strain)} = \frac{\sum_{g=1}^{n_g}\sum_{f=1}^{n_f}\sum_{s=1}^{n_s}\left(\left|\dot{\gamma}_s^f\right|\cdot v_g\right)}{\bar{\dot{\varepsilon}}} \quad . \tag{11}$$

By doing so, the *M* factors for strains (Eq. 8) and for stresses (Eq. 9) are always equal. The reason for using one or the other depends on what physical quantity is required to be converted between the macroscopic and microscopic levels.

What is needed for the polycrystal simulation is to obtain the values of the microscopic hardening parameters appearing in Eq. (1) (τ_0, h_c , a_c , τ_{sat}) from the macroscopic ones in Eq. (4) (σ_{00}, *h*, *a* and σ_{sat}). Using the Taylor factor defined in Eq. (9) for stresses, the transformation formulas are:

$$\tau_0 = \sigma_{00}/M, \tag{12}$$

$$\tau_{sat} = \sigma_{sat}/M, \tag{13}$$

$$h_c = h/M^2, \tag{14}$$

$$a_c = a\ . \tag{15}$$

First, we examine how to apply these formulas when there is only one slip system family that contributes to the plastic deformation. The Taylor factor can be determined using the polycrystal plasticity code just by doing a single small strain increment, and applying Eq. (9). In such a calculation, the value of τ_0 can be arbitrary because *M* is the ratio of the macroscopic flow stress and the resolved shear stress, while the macroscopic stress is proportional to the resolved shear stress. Having the Taylor factor, all microscopic strain hardening parameters can be obtained by employing Eqs. (12-14), and a full simulation can be done. Nevertheless, before starting a full simulation, it is useful to verify that the macroscopic yield stress is reproduced by the employed Taylor factor. Thus, a single step simulation is required to verify that σ_{00} is actually reproduced by the VPSC simulation. This is not guaranteed because a uniform τ_0 value is used for each grain, while in the real material, the physical quantities are never so ideally homogeneous as in the simulations. Besides, there can be also differences in the grain shapes, or initial texture, both leading to deviations in the Taylor factor of the real material and the simulated one. For all these

possible reasons, an adjustment of the Taylor factor might be needed to assure that Eq. (12) becomes valid. This adjustment is simply a multiplication of the simulated Taylor factor by the ratio of the second and the first simulated yield stresses. Once this step is achieved, M and τ_0 are known, and one can determine the other three microscopic parameters using Eqs. (13-15). After this, a full simulation can be performed by the polycrystal code to obtain the macroscopic stress response of the polycrystal. If needed, minor adjustments of the parameter values can still be done to reproduce the experimental measurements better. In the applications presented in this work, only the value of τ_{sat} was needed to be slightly changed to fit the curves well at higher strains. Concerning the self and latent hardening parameters (q_c^{ij}), earlier simulation works have led to general constant values by grouping them into four categories [19], according to the geometrical relation between the slip systems: $q_c^{(1)}$=1 for coplanar slip, $q_c^{(2)}$=1.2 for collinear slip, $q_c^{(3)}$=1.4 for perpendicular slip, and $q_c^{(4)}$=1.2 for all other geometrical situations. These values were used for all simulation cases.

On the other hand, assigning the microscopic hardening parameters is a more complex task when several slip system families are active in the material. In this case, the following strategy was adopted in the present work. For the n_f number of families, there are n_f number of τ_0^i and τ_{sat}^i values (i =1... n_f). Previous simulation works have led to a set of τ_0^i values, so in the first attempt, they were adopted for calculating the yield stress of the material. In case of difference between the simulated and experimental macroscopic yield stress, the τ_0^i values were scaled proportionally so that the yield stress were the same. This procedure permitted also to obtain a Taylor factor which was then used for calculating the other parameters. Concerning τ_{sat}^i, a single value was assigned for each slip system family, according to Eq. (13).

The VPSC polycrystal code in its version developed by Molinari and Toth [47] was employed to predict the Taylor factor (M) as well as to simulate the mechanical response of the polycrystal in the form of stress-strain curves. To constitute the polycrystal, 6000 grain orientations were selected from the measured texture (when it was available), or a random texture was used if the initial texture was not known. For this purpose, the ATEX software [48] was used for the discretization procedure. The strain rate sensitivity index (m) of slip

was taken as 0.05 and the α coefficient in the localization law of the self-consistent model was 0.7 (see Molinari and Toth [47] for the details of the VPSC approach used). The flow stress was obtained from the macroscopic stress and strain rate tensors as a work conjugate quantity to the von-Mises equivalent strain rate $\dot{\bar{\varepsilon}}_c$:

$$\bar{\sigma}_c = \left(\underline{\underline{\sigma}}_c : \underline{\underline{\dot{\varepsilon}}}_c\right) / \dot{\bar{\varepsilon}}_c . \tag{16}$$

(Note that here $\bar{\sigma}_c$ is not a von-Mises equivalent stress as the polycrystal is not an isotropic von-Mises material.) Subsequently, the stress-strain curves were plotted using $\bar{\sigma}_c$ as a function of $\bar{\varepsilon}_c$.

5. Results

The new analytical strain hardening function presented in Eq. (4) was tested for different deformation modes and for materials exhibiting different forms of crystal structures, such as face-centered cubic (FCC), body-centered cubic (BCC) and hexagonal closed packed (HCP). The considered deformation modes were uniaxial tension, compression and torsion testing. The experimental results for evaluating the mechanical response of the materials were adopted from published literature on aluminum [24,49], commercially pure (CP) copper (C110) [50], low carbon steel [22] and titanium (CP-grade 2) [51]. This includes deformation ranging from intermediate to high strain levels. The experimental curves were reproduced in Fig. 1a for aluminum (Al 2024 in T351 state) subjected to uniaxial tension, compression and torsion [49], in Fig. 1b for uniaxial tensile test of copper (C110) [50] as well as for low carbon steel [22]. Fig. 1c presents the stress-strain curve for high torsion strain level for aluminum (Al 1050) [24] and for copper (C110) [50]. Fig. 1d displays the case of HCP-Ti (CP-grade 2) alloys under uniaxial tensile tests at room temperature (RT) and at 300°C [51].

For all these above-mentioned cases, the macroscopic parameters were first determined using the presented minimization technique and a comparison of the fitting curves with the experimental ones was accomplished, as discussed in Sec. 5.1. Subsequently, the macroscopic parameters obtained from the analytical approach were transformed into the

337 microscopic ones, i.e., to the grain level, and then simulations were performed using the
338 VPSC code to predict the strain hardening responses, see Sec. 5.2.

339 **5.1. Results obtained from fitting the mechanical response by the phenomenological**
340 **hardening function**

341 Fig. 1 presents the fitted stress-strain responses obtained using the analytical
342 hardening function (Eq. 4) in comparison with the experimental counterparts for the different
343 sets of materials mentioned above under different loading conditions, i.e., tension,
344 compression and torsion. It can be seen that the analytical hardening function (identified as
345 'fitted' in Fig. 1), precisely captures the experimental stress-strain curves. One can appreciate
346 the quality of the fitted stress-strain plots by the analytical hardening function by the fact that
347 we are using only four parameters (i.e., σ_{00} , σ_{sat} , h and a), to reproduce the entire plastic
348 part of the strain hardening curve. Table 1 summarizes the fitted hardening parameters for
349 each of the curves presented in Fig. 1.

350 **5.2. Predicting strain hardening using the VPSC crystal plasticity approach**

351 Figs. 2-5 present the predicted mechanical response and the corresponding strain
352 hardening rate plots obtained by VPSC simulations in comparison with experiments. Results
353 are shown first for the lower strain regime for different strain paths in Fig. 2 for aluminum,
354 and in Fig. 3 for copper and steel. The results for large strain hardening in torsion are
355 presented in Fig. 4 for copper and aluminum. A representative example is also shown for
356 hexagonal crystal structure; for Titanium, see Fig. 5, for two cases: tension parallel (Fig. 5b-
357 c) and perpendicular (Fig. 5d-e) to the rolling direction of the sheet from which the tensile
358 sample was cut. Whenever the experimental initial texture was available (as indicated in
359 Table 2), it was used in the form of a polycrystal with 6000 grains for the VPSC polycrystal
360 simulations; they are also shown in the figures in form of pole figures. When the initial
361 texture was unknown, a random texture was used, also with 6000 grains. One can see that the
362 VPSC simulations reproduce perfectly the experimental curves, just like the
363 phenomenological fitting as shown in Fig. 1.

364 As there is very good agreement between the VPSC-simulated and experimental
365 strain hardening curves, the agreement is also good for their derivatives; $\theta = d\bar{\sigma}/d\bar{\varepsilon}$, which
366 constitutes the so-called Kocks-Mecking plot as a function of stress, see in Figs. 2-5. The

367 well-known Stage III and IV hardening stages are indicated for the case of copper and
368 aluminum in Fig. 4.

369

370 ## 6. Discussion

371 As the present work has two major parts, we first discuss about the new
372 phenomenological function, and then the crystal plasticity simulations will be examined.
373 Finally, the discussion part will be closed with an evaluation of the applicability conditions
374 for both of these approaches.

375 ### 6.1. Discussion on the new phenomenological strain hardening function

376 The new strain hardening function has four parameters, which is a relatively low
377 number with respect to other propositions (for example, the recent modified Ludwigson
378 function [7] has six parameters). In order to obtain the values of the parameters, we
379 established a rapid minimization procedure using about 50 representative points from the
380 experimental curve (Section 3).

381 It is also important to compare the performance of the new proposed
382 phenomenological hardening function to that of existing ones. In this regard, we have carried
383 out such comparisons with two previous propositions: with Chinh et al. [3], and with
384 Lavakumar et al. [7]. Chinh et al. [3] presented a mixed exponential power-law empirical
385 relation for reproducing especially the asymptotic limiting stage (see their equation in Fig.
386 6a). The fitted hardening curves in Fig. 6b correspond to the same experimental curves but
387 obtained by the present phenomenological approach. As can be seen, the agreement is better
388 with the present approach, while both approaches use the same number of parameters (four).

389 Lavakumar et al. [7] proposed a modification to the Ludwigson [1] equation which is
390 a mixed power-law and exponential function (see the function in Fig. 7a). They reproduced
391 satisfactorily the strain hardening behavior of various metallic materials when deformed to a
392 low strain regime (Fig. 7a). We applied our function as well on the same data basis; see the
393 results in Fig. 7b. Closer inspection reveals that our function approaches the experimental
394 curves in better accordance by using only four parameters as compared to six in the modified
395 Ludwigson function.

396 ### 6.2. Discussion on the crystal plasticity simulations

Tables 3-6 lists the parameters used for predicting the mechanical response using the VPSC approach. They were obtained from the phenomenological analysis by transforming the parameters to the grain level with the help of the Taylor factor. The adjusted Taylor factors are presented in Table 2 together with the simulated Taylor factors (the latter in parenthesis). The difference between the Taylor factors was pointed out in Section 4 above; possibly due to the non-uniform initial strengths of the slip systems in the material, the crystallographic texture (if was not known, so a random texture was used), or the differences in the assumed and experimental grain shapes. Table 2 presents also the values of the λ parameter, which expresses the ratio of the external plastic power to the 'apparent internal' one (which is the sum of the individual grain-powers). This issue was also examined in the recent work of Sahoo et al. [46] where the strain hardening behavior of two-phase composites were modeled using a plastic power-based composite approach. The range of λ found in the present work is between 1.06 and 1.16, which is quite similar to the range found in Sahoo et al. [46]. λ is always larger than 1.0, meaning that the 'apparent internal plastic power' calculated within the grains is less than the macroscopic plastic power. As discussed in Sahoo et al. [46], the origin of this unbalance of plastic powers can be attributed to the non-uniform distribution of the stress and strain within the components of the composite, that is, within the grain-interiors of the polycrystal.

6.3. Model limitations

The present modeling is presented for two levels: at the macroscopic level, where the hardening function is totally empirical, and at grain level, for crystal plasticity simulations. The limitations of these two modeling have to be discussed for both the conditions. For the phenomenological case, the function can describe continuous hardening (also continuous softening). As no information is used on the metallurgical state of the metal in the parameter fitting, the parameters are not directly related to a specific material state. Nevertheless, as the proposed function is able to capture the strain hardening response of the material up to large strains (see the torsion example) where significant microstructural evolution is taking place, somehow the parameters are related to those changes. They are: evolution in dislocation density, changes in dislocation cell-size (for alloys showing dislocation cell structures), variation in grain size due to grain fragmentation, or texture evolution due to deformation.

On the contrary, for the crystal plasticity modeling, only crystallographic glide was used as a possible deformation mechanism, so the application is more limited. For that case, it

is implicitly assumed that the metallurgical state of the alloy does not change during deformation due to phase transformations, twinning or recrystallization. It is designed actually for isothermal conditions and constant strain rate, and not applicable when twinning, phase transformation or dynamic recrystallization is taking place during plastic deformation.

7. Summary

The subject of this work is to propose a new strain hardening function with a small number of parameters for use in engineering applications. The new function is based on an earlier crystal plasticity-based hardening function proposed to describe the self and latent hardening of single crystals. It has been successfully applied to several polycrystalline metals with different crystallographic structures and compared with previous approaches. The proposed hardening function has the significant advantage of containing parameters that can be transformed into crystal plasticity parameters, thereby permitting them to be used directly in polycrystal plasticity simulations. This conversion is based on the Taylor factor of the polycrystal. Using these parameters in the VPSC polycrystal model, one can obtain an accurate simulation of the strain hardening curve, like the one obtained by the phenomenological crystal plasticity-based analytical hardening function. It was also shown in this work that there are two kinds of Taylor factors; one for converting the strain and another for the stress quantities between the macroscopic and the grain levels. While they have the same values, their formulas are different; the stress-Taylor factor contains a parameter (λ) which is related to the energy balance between the external and 'apparent internal plastic power'. This parameter, however, can be readily obtained from the stress and strain quantities computed during the crystal plasticity simulation, and thus the conversion for the stresses is straightforward.

8. Acknowledgement

This work was supported by the National Research Agency, France, referenced as ANR-11-LABX-008-01 (LabEx DAMAS). Viet Q. Vu acknowledges the PhD scholarship awarded by the Vietnamese Government (Project 911).

459 # Appendix

460 ## Taylor factor

461 The Taylor factor is employed to bridge the differences between two scales: the macroscopic
462 one and the grain level. It can also be used for linking either the strains or stresses. The grain
463 is a crystal which deforms by slip on several slip systems simultaneously. First, we define the
464 Taylor factor for a single grain, and then for a polycrystal.

465 *Taylor factor for single crystals*

466 The slip systems are grouped into families in a grain, according to their common features. We
467 denote the number of families by n_f and the number of slip systems within one family by n_s
468 (the *f* index stands for 'family', and the *s* for slip). The basis for establishing the Taylor
469 factor is the equality of the 'internal' and 'external' plastic power in unit volume:

470 $$\sum_{f=1}^{n_f}\sum_{s=1}^{n_s}\tau_s^f\dot{\gamma}_s^f = \sigma_{kl}\dot{\varepsilon}_{kl} \quad . \tag{A1}$$

471 Here τ_s^f is the resolved shear stress on a slip system, σ_{kl} is the stress tensor and $\dot{\varepsilon}_{kl}$ is the
472 strain rate tensor. The latter tensorial quantities can be changed into scalars, where $\bar{\dot{\varepsilon}}$ is the
473 von-Mises equivalent strain rate, and $\bar{\sigma}$ is the equivalent stress:

474 $$\sum_{f=1}^{n_f}\sum_{s=1}^{n_s}\tau_s^f\dot{\gamma}_s^f = \bar{\sigma}\cdot\bar{\dot{\varepsilon}} \quad . \tag{A2}$$

475 Note that $\bar{\sigma}$ is not the von-Mises equivalent stress (because a crystal is not an isotropic
476 material); it is the work-conjugate equivalent stress.

477 Using the slip rates, first we define the *average resolved shear stress* $\bar{\tau}_r$:

478 $$\bar{\tau}_r = \sum_{f=1}^{n_f}\sum_{s=1}^{n_s}\tau_s^f\dot{\gamma}_s^f \Big/ \sum_{f=1}^{n_f}\sum_{s=1}^{n_s}\left|\dot{\gamma}_s^f\right| \quad . \tag{A3}$$

479 Eq. (A2) now becomes:

$$\overline{\tau}_r \cdot \sum_{f=1}^{n_f} \sum_{s=1}^{n_s} \left\| \dot{\gamma}_s^f \right\| = \overline{\sigma} \cdot \overline{\dot{\varepsilon}} \quad . \tag{A4}$$

Using this equation, the Taylor factor M_g for a grain 'g' can now be defined in two forms, one for the strains, and another for the stresses:

$$M_g^{(strain)} = \frac{\sum_{f=1}^{n_f} \sum_{s=1}^{n_s} \left\| \dot{\gamma}_s^f \right\|}{\overline{\dot{\varepsilon}}} \quad , \quad M_g^{(stress)} = \frac{\overline{\sigma}}{\overline{\tau}_r} . \tag{A5a,b}$$

Note that these two kinds of Taylor factors have the same values. In crystal plasticity simulations, the Taylor factor can be readily calculated when all quantities needed for its definition are available. Note that in the work of Mecking et al. [52], Taylor factors were defined for single crystals, similarly to the present work, designed for strain and stress (Eqs. 5a,b); however, they were defined independently, resulting in disparities in values and making inconsistencies when they were employed.

Taylor factor for polycrystals

For polycrystals, the material has to be considered as a composite, made of single crystals of the same material with number of components equal to the number of grains. The grains are anisotropic, so the difference between adjacent grains is coming from their anisotropic mechanical behavior. For a composite material, the equality of the internal and external powers can only be used as volume integrals (Hill's lemma), contrary to the case of a single-phase material (i.e., the single crystal), where the plastic power can be calculated by the average values of stress and strain rate. First, we write the energy integral for the polycrystal in the following two forms:

$$\sum_{g=1}^{n_g} \int_{V_g} \underline{\underline{\sigma}}_g(\underline{r}) : \underline{\underline{\dot{\varepsilon}}}_g(\underline{r}) \cdot dV_g = \int_V \underline{\underline{\sigma}}(\underline{r}) : \underline{\underline{\dot{\varepsilon}}}(\underline{r}) \cdot dV \quad . \tag{A6}$$

Here, $\underline{\underline{\sigma}}_g(\underline{r})$ and $\underline{\underline{\dot{\varepsilon}}}_g(\underline{r})$ are the position dependent stress tensor and strain rate tensors in a grain 'g', while $\underline{\underline{\sigma}}(\underline{r})$, $\underline{\underline{\dot{\varepsilon}}}(\underline{r})$ are actually the same, without distinguishing the grains. V_g is the volume of a grain, and V is the total volume of the polycrystal. According to Hill's

lemma, the volume integral on the right side of Eq. (A6) can be replaced with the multiplication of the volume averages of the stress and strain rate tensors ($\underline{\underline{\sigma}}_c$, $\underline{\underline{\dot{\varepsilon}}}_c$):

$$\int_V \underline{\underline{\sigma}}(\underline{r}) : \underline{\underline{\dot{\varepsilon}}}(\underline{r}) \cdot dV = \left(\int_V \underline{\underline{\sigma}}(\underline{r}) \cdot dV \right) : \left(\int_V \underline{\underline{\dot{\varepsilon}}}(\underline{r}) \cdot dV \right) . \tag{A7}$$

These volume integrals can be done grain by grain, so one can write:

$$\int_V \underline{\underline{\sigma}}(\underline{r}) \cdot dV = \sum_{g=1}^{n_g} \int_{V_g} \underline{\underline{\sigma}}_g(\underline{r}) \cdot dV_g = \sum_{g=1}^{n_g} \overline{\underline{\underline{\sigma}}}_g \cdot V_g = V \cdot \underline{\underline{\sigma}}_c \ , \tag{A8}$$

$$\int_V \underline{\underline{\dot{\varepsilon}}}(\underline{r}) \cdot dV = \sum_{g=1}^{n_g} \int_{V_g} \underline{\underline{\dot{\varepsilon}}}_g(\underline{r}) \cdot dV_g = \sum_{g=1}^{n_g} \overline{\underline{\underline{\dot{\varepsilon}}}}_g \cdot V_g = V \cdot \underline{\underline{\dot{\varepsilon}}}_c \ , \tag{A9}$$

where $\overline{\underline{\underline{\sigma}}}_g$, $\overline{\underline{\underline{\dot{\varepsilon}}}}_g$ are the average stress and strain rate tensors within a grain indexed by g; $\underline{\underline{\sigma}}_c$, $\underline{\underline{\dot{\varepsilon}}}_c$ are the macroscopic stress and strain tensors, respectively and n_g is the number of grains in the polycrystal. The right-hand side of Eq. (A6) can be called the macroscopic plastic power (P_c), so the energy balance expressed in Eq. (A6) can be rewritten as:

$$\sum_{g=1}^{n_g} \int_{V_g} \underline{\underline{\sigma}}_g(\underline{r}) : \underline{\underline{\dot{\varepsilon}}}_g(\underline{r}) \cdot dV_g = V \cdot \underline{\underline{\sigma}}_c : \underline{\underline{\dot{\varepsilon}}}_c = P_c \ . \tag{A10}$$

On the other hand, Hill's lemma does not apply to the individual grains within the polycrystal as a composite, so there is an inequality when one writes the following:

$$\sum_{g=1}^{n_g} \int_{V_g} \underline{\underline{\sigma}}_g(\underline{r}) : \underline{\underline{\dot{\varepsilon}}}_g(\underline{r}) \cdot dV_g \neq \sum_{g=1}^{n_g} \left(\int_{V_g} \underline{\underline{\sigma}}(\underline{r}) \cdot dV_g \right) : \left(\int_{V_g} \underline{\underline{\dot{\varepsilon}}}(\underline{r}) \cdot dV_g \right) = \hat{P} \ . \tag{A11}$$

The right-hand side of this equation will be called hereafter the 'apparent internal plastic power'; $\hat{P}$. The two integrals in Eq. (A11) are the average stress and strain values of the stresses and strain rates within individual grains of the polycrystal, so $\hat{P}$ can be written as:

$$\hat{P} = \sum_{g=1}^{n_g} \overline{\underline{\underline{\sigma}}}_g : \overline{\underline{\underline{\dot{\varepsilon}}}}_g \cdot V_g \ . \tag{A12}$$

In a polycrystal plasticity modeling, both P_c and $\hat{P}$ can be calculated, so by introducing a scalar parameter (λ) between them, we can write:

$$\lambda \hat{P} = P_c \ . \tag{A13}$$

The value of λ is a measure of the deviation between the 'external plastic power' and the 'apparent internal plastic power':

$$\lambda = \frac{\underline{\underline{\sigma}}_c : \dot{\underline{\underline{\varepsilon}}}_c}{\sum_{g=1}^{n_g} \underline{\underline{\bar{\sigma}}}_g : \dot{\underline{\underline{\bar{\varepsilon}}}}_g \cdot v_g} \ . \tag{A14}$$

Here v_g is the volume fraction of a grain: $v_g = V_g / V$. As λ is defined by Eq. (A14), and all quantities are available to calculate its value from a polycrystal plasticity code, the value of λ can be calculated by Eq. (A14).

Now the apparent plastic power $\hat{P}$, defined by (A12), is rewritten for the polycrystal using the resolved shear stresses and resolved shear strain rates:

$$\hat{P} = V \cdot \sum_{g}^{n_g} \sum_{f=1}^{n_f} \sum_{s=1}^{n_s} \left(\tau_s^f \cdot \dot{\gamma}_s^f \cdot v_g \right) \ . \tag{A15}$$

This is done in order to replace the tensorial quantities with scalar ones. Similar change can be done also for the external plastic power, P_c. Using its expression given by the right-hand side of Eq. (A10), we write:

$$P_c = V \cdot \underline{\underline{\sigma}}_c : \dot{\underline{\underline{\varepsilon}}}_c = V \cdot \bar{\sigma}_c \cdot \dot{\bar{\varepsilon}}_c \ , \tag{A16}$$

where $\dot{\bar{\varepsilon}}_c$ is the von-Mises equivalent strain rate, and $\bar{\sigma}_c$ is the work-conjugate equivalent stress, defined by Eq. (A16):

$$\bar{\sigma}_c = \frac{\underline{\underline{\sigma}}_c : \dot{\underline{\underline{\varepsilon}}}_c}{\dot{\bar{\varepsilon}}_c} \ , \tag{A17}$$

Then Eq. (A13) can be written as:

$$\lambda \cdot \sum_{g}^{n_g} \sum_{f=1}^{n_f} \sum_{s=1}^{n_s} \left(\tau_s^f \cdot \dot{\gamma}_s^f \cdot v_g \right) = \bar{\sigma}_c \cdot \bar{\dot{\varepsilon}}_c \quad . \tag{A18}$$

Similar to the case of single crystal, the expression of the average resolved shear stress $\bar{\tau}_r$ for a polycrystal becomes:

$$\bar{\tau}_r = \sum_{g=1}^{n_g} \sum_{f=1}^{n_f} \sum_{s=1}^{n_s} \left(\tau_s^f \cdot \dot{\gamma}_s^f \cdot v_g \right) \Big/ \sum_{g=1}^{n_g} \sum_{f=1}^{n_f} \sum_{s=1}^{n_s} \left(\left| \dot{\gamma}_s^f \right| \cdot v_g \right) \quad . \tag{A19}$$

Eq. (A18) is written then:

$$\lambda \cdot \bar{\tau}_r \cdot \sum_{g=1}^{n_g} \sum_{f=1}^{n_f} \sum_{s=1}^{n_s} \left(\left| \dot{\gamma}_s^f \right| \cdot v_g \right) = \bar{\sigma}_c \cdot \bar{\dot{\varepsilon}}_c \quad . \tag{A20}$$

From this, the Taylor factor *M* for polycrystals is calculated in its two forms as:

$$M^{(strain)} = \frac{\sum_{g=1}^{n_g} \sum_{f=1}^{n_f} \sum_{s=1}^{n_s} \left(\left| \dot{\gamma}_s^f \right| \cdot v_g \right)}{\bar{\dot{\varepsilon}}} \quad , \quad M^{(stress)} = \frac{\bar{\sigma}}{\lambda \cdot \bar{\tau}_r} , \tag{A21a,b}$$

where λ is computed from Eq. (A14). Note that the values of these two Taylor factors are the same. These definitions can be used in any polycrystal model as there was no implied assumption in its definition on the uniformity of strain (Taylor model), or the stress (Static model), or heterogeneous deformation (Self-consistent model, where both stress and strain in a grain can be different from the macroscopic ones).

Figure Captions:

Fig. 1. Fitted stress-strain response obtained from analytical phenomenological hardening curve, compared to measurements.

Fig. 2. VPSC simulation results for aluminum (Al 2024) in comparison with experimental measurements for (a) stress-strain response and (b) strain hardening rate.

Fig. 3. Initial input texture used for VPSC simulation for (a) Steel and (b) Copper (C110). Comparative plots of both the experimental and predicted (c) stress-strain response and (d) strain hardening rate behavior of both the tested specimens obtained from the VPSC simulation.

Fig. 4. Initial input texture used for VPSC simulation for (a) Aluminum (Al 1050) and (b) Copper (C110). Comparative plots of both the experimental and predicted (c) stress-strain response and (d-e) strain hardening rate behavior of both the tested specimens obtained from the VPSC simulation.

Fig. 5. Initial input texture used for VPSC simulation for (a) rolled titanium (CP-grade 2) sample similar to the published literature (Orozco-Caballero et al., 2018).
(b-e) Comparative plots of both the experimental and predicted stress-strain response and strain hardening rate behavior obtained from the VPSC simulation for tension parallel and perpendicular to the rolling direction at room temperature and 300°C.

Fig. 6. Comparison of the strain hardening plots between (a) the function of Chinh et al. (2004) and (b) the proposed analytical phenomenological function.

Fig. 7. Comparison of the strain hardening plots between (a) the modified Ludwigson function (Lavakumar et al. (2021)), and (b) the proposed analytical phenomenological function.

Table Captions:

Table 1. The hardening parameters obtained by fitting the new phenomenological hardening law for different materials and testing conditions.

Table 2. The predicted and the adjusted values of the Taylor factor for different materials, the λ parameter and the test conditions obtained by VPSC simulation.

Table 3. The hardening parameters used in the VPSC simulations to fit the phenomenological hardening law corresponding to different materials and test conditions.

Table 4. The hardening parameters used in the VPSC simulation to fit the phenomenological hardening law corresponding to steel.

Table 5. The hardening parameters for HCP-Ti tensile testing used in VPSC simulations.

Table 6. Initial Reference Resolved Shear Stresses for hexagonal slip system families, in [MPa].

References

[1] D.C. Ludwigson, Modified stress-strain relation for FCC metals and alloys, Metall. Trans. 2 (1971) 2825-2828, doi:10.1007/bf02813258.

[2] Y. Estrin, L.S. Tóth, A. Molinari, Y. Bréchet, A dislocation-based model for all hardening stages in large strain deformation, Acta Mater. 46 (1998) 5509-5522, doi:10.1016/s1359-6454(98)00196-7.

[3] N.Q. Chinh, G. Horváth, Z. Horita, T.G. Langdon, A new constitutive relationship for the homogeneous deformation of metals over a wide range of strain, Acta Mater. 52 (2004) 3555-3563, doi:10.1016/j.actamat.2004.04.009.

[4] L.S. Tóth, Y. Estrin, R. Lapovok, C. Gu, A model of grain fragmentation based on lattice curvature, Acta Mater. 58 (2010) 1782-1794, doi:10.1016/j.actamat.2009.11.020.

[5] P. Les, H.P. Stuewe, M. Zehetbauer, Hardening and strain rate sensitivity in stage IV of deformation in f.c.c. and b.c.c. metals, Mater. Sci. Eng. A 234-236 (1997) 453-455, doi:10.1016/s0921-5093(97)00259-1.

[6] B.K. Choudhary, J. Christopher, Stage-II tensile work hardening behaviour of type 316L(N) austenitic stainless steel, Mater. Sci. Eng. A 651 (2016) 486-489, doi:10.1016/j.msea.2015.11.001.

[7] A. Lavakumar, S.S. Sarangi, V. Chilla, D. Narsimhachary, R.K. Ray, A “new” empirical equation to describe the strain hardening behavior of steels and other metallic materials, Mater. Sci. Eng. A 802 (2021) 140641, doi.org/10.1016/j.msea.2020.140641.

[8] D.A. Hughes, N. Hansen, The microstructural origin of work hardening stages, Acta Mater. 148 (2018) 374-383, doi:10.1016/j.actamat.2018.02.002.

[9] P. Ludwik, Elemente der Technologischen mechanic (1909), doi.org/10.1007/978-3-662-40293-1.

[10] J.H. Hollomon, 1945. Met. Technol. XII (1945). June 1945 - Tensile Deformation, 879 (1945) 268-290.

[11] H.W. Swift, Plastic instability under plane stress, J. Mech. Phys. Solids 1 (1952) 1-18, doi:10.1016/0022-5096(52)90002-1.

[12] E. Voce, A practical strain hardening function, Metallurgia, 51 (1955) 219-226.

[13] G.R. Johnson, W.H. Cook, Fracture characteristics of three metals subjected to various strains, strain rates, temperatures and pressures, Eng. Fract. Mech. 21 (1985) 31-48, doi:10.1016/0013-7944(85)90052-9.

[14] U.F. Kocks, Laws for work-hardening and low-temperature creep, J. Eng. Mater. Technol. 98 (1976) 76, doi:10.1115/1.3443340.

[15] H. Mecking, U.F. Kocks, Kinetics of flow and strain-hardening, Acta Metall. 29 (1981) 1865-1875, doi:10.1016/0001-6160(81)90112-7.

[16] Y. Estrin, H. Mecking, A unified phenomenological description of work hardening and creep based on one-parameter models, Acta Metall. 32 (1984) 57-70, doi:10.1016/0001-6160(84)90202-5.

[17] R. Hill, Generalized constitutive relations for incremental deformation of metal crystals by multislip, J. Mech. Phys. Solid. 14 (1966) 95-102, doi:10.1016/0022-5096(66)90040-8.
[18] S.R. Kalidindi, C.A. Bronkhorst, L. Anand, Crystallographic texture evolution in bulk deformation processing of FCC metals, J. Mech. Phys. Solids 40 (1992) 537-569, doi:10.1016/0022-5096(92)80003-9.
[19] Y. Zhou, K.W. Neale, L.S. Tóth, A modified model for simulating latent hardening during the plastic deformation of rate-dependent FCC polycrystals, Int. J. Plast. 9 (1993), 961-978, doi:10.1016/0749-6419(93)90061-t.
[20] P. Franciosi, A. Zaoui, Multislip in f.c.c. crystals a theoretical approach compared with experimental data, Acta Metall. 30 (1982) 1627-1637, doi:10.1016/0001-6160(82)90184-5.
[21] X. Wu, S. Kalidindi, C. Necker, A. Salem, Prediction of crystallographic texture evolution and anisotropic stress-strain curves during large plastic strains in high purity α-titanium using a Taylor-type crystal plasticity model, Acta Mater. 55 (2007) 423-432, doi:10.1016/j.actamat.2006.08.034.
[22] S.S. Dhinwal, L.S. Toth, Unlocking deformation path in asymmetric rolling by texture simulation, Materials 13 (2019) 101, doi:10.3390/ma13010101.
[23] S.K. Sahoo, L.S. Toth, S. Biswas, An analytical model to predict strain-hardening behaviour and twin volume fraction in a profoundly twinning magnesium alloy, Int. J. Plast. 119 (2019) 273-290, doi:10.1016/j.ijplas.2019.04.007.
[24] V.Q. Vu, L.S. Toth, Y. Beygelzimer, R. Kulagin, A.H. Kobaissy, Modelling of crystallographic texture in plastic flow machining, Adv. Eng. Materials (2019) 1900661, doi:10.1002/adem.201900661.
[25] P.B. Hirsch, J.S. Lally, The deformation of magnesium single crystals, Philos. Mag. 12 (1965) 595-648, doi:10.1080/14786436508218903.
[26] S. Breumier, S. Sao-Joao, A. Villani, M. Lévesque, G. Kermouche, High strain rate micro-compression for crystal plasticity constitutive law parameters identification, Mater. Des. 193 (2020) 1-17, doi.org/10.1016/j.matdes.2020.108789.
[27] S. Gupta, A.J. Beaudoin, J. Chevy, Strain rate jump induced negative strain rate sensitivity (NSRS) in aluminum alloy 2024: Experiments and constitutive modeling, Mater. Sci. Eng. A 683 (2017) 143-152.
[28] V. Herrera-Solaz, J. LLorca, E. Dogan, I. Karaman, J. Segurado, An inverse optimization strategy to determine single crystal mechanical behavior from polycrystal tests: Application to AZ31 Mg alloy, Int. J. Plast. 57 (2014) 1-15, doi:10.1016/j.ijplas.2014.02.001.
[29] R. Mahnken, E. Stein, A unified approach for parameter identification of inelastic material models in the frame of the finite element method, Comput. Meth. Appl. Mech. Eng. 136 (1996) 225-258, doi:10.1016/0045-7825(96)00991-7.
[30] K. Sedighiani, M. Diehl, K. Traka, F. Roters, J. Sietsma, D. Raabe, An efficient and robust approach to determine material parameters of crystal plasticity constitutive laws from macro-scale stress-strain curves, Int. J. Plast. (2020) 102779, doi.org/10.1016/j.ijplas.2020.102779.

[31] D. Wicht, M. Schneider, T. Böhlke, An efficient solution scheme for small-strain crystal-elasto-viscoplasticity in a dual framework, Comput. Meth. Appl. Mech. Eng. 358 (2020) 112611, doi.org/10.1016/j.cma.2019.112611.
[32] C. Zambaldi, Y. Yang, T.R. Bieler, D. Raabe, Orientation informed nanoindentation of α-titanium: Indentation pileup in hexagonal metals deforming by prismatic slip, J. Mater. Res. 27 (2011) 356-367, doi:10.1557/jmr.2011.334.
[33] Y. Liu, B. Wang, M. Yoshino, S. Roy, H. Lu, R. Komanduri, Combined numerical simulation and nanoindentation for determining mechanical properties of single crystal copper at mesoscale, J. Mech. Phys. Solids 53 (2005) 2718-2741, doi:10.1016_j.jmps.2005.07.003.
[34] B. Eidel, Crystal plasticity finite-element analysis versus experimental results of pyramidal indentation into (001) fcc single crystal, Acta Mater. 59(2011) 1761-1771, doi:10.1016/j.actamat.2010.11.042.
[35] D.K. Patel, S.R. Kalidindi, Correlation of spherical nanoindentation stress-strain curves to simple compression stress-strain curves for elastic-plastic isotropic materials using finite element models, Acta Mater. 112 (2016) 295-302, doi:10.1016/j.actamat.2016.04.034.
[36] S. Mandal, B.T. Gockel, A.D. Rollett, Application of canonical correlation analysis to a sensitivity study of constitutive model parameter fitting, Mater. Des. 132 (2017) 30-43, doi: 10.1016/j.matdes.2017.06.050.
[37] A. Chakraborty, P. Eisenlohr, Evaluation of an inverse methodology for estimating constitutive parameters in face-centered cubic materials from single crystal indentations, Eur. J. Mech. A/Solids 66 (2017) 114-124, doi:10.1016/j.euromechsol.2017.06.012.
[38] A. Guery, F. Hild, F. Latourte, S. Roux, Identification of crystal plasticity parameters using DIC measurements and weighted FEMU, Mechanics of Materials 100 (2016) 55-71, doi:10.1016/j.mechmat.2016.06.007.
[39] L. Cauvin, B. Raghavan, S. Bouvier, X. Wang, F. Meraghni, Multi-scale investigation of highly anisotropic zinc alloys using crystal plasticity and inverse analysis, Mater. Sci. Eng. A 729 (2018) 106-118, doi:10.1016/j.msea.2018.05.038.
[40] R.A. Lebensohn, C.N. Tomé, A self-consistent anisotropic approach for the simulation of plastic deformation and texture development of polycrystals: Application to zirconium alloys, Acta Metall. 41 (1993) 2611-2624, doi:10.1016/0956-7151(93)90130-k.
[41] H. Kim, F. Barlat, Y. Lee, S.B. Zaman, C.S. Lee, Y. Jeong, A crystal plasticity model for describing the anisotropic hardening behavior of steel sheets during strain-path changes, Int. J. Plast. 111 (2018) 85-106, doi:10.1016/j.ijplas.2018.07.010.
[42] X.Q. Guo, C. Ma, H. Wang, X.B. Mao, P.D. Wu, Numerical study of large strain behavior of OFHC copper: The role of latent hardening, Mater. Sci. Eng. A 744 (2019) 386-395, doi:10.1016/j.msea.2018.12.028.
[43] S. Ghorbanpour, Md E. Alam, N.C. Ferreri, A. Kumar, B.A. McWilliams, S.C. Vogel, J. Bicknell, I.J. Beyerlein, M. Knezevic, Experimental characterization and crystal plasticity modeling of anisotropy, tension-compression asymmetry, and

texture evolution of additively manufactured Inconel 718 at room and elevated temperatures, Int. J. Plast. 125 (2020) 63-79, doi:10.1016/j.ijplas.2019.09.002.
[44] Ali Al-Hadi Ayoub Kobaissy, G. Ayoub, W. Nasim, J. Malik, I. Karaman, M. Shehadeh, Modeling of the ECAP induced strain hardening behavior in FCC metals, Metall. Mater. Trans. A Phys. Metall. Mater. Sci. 51 (2020) 5453-5474, doi.org/10.1007/s11661-020-05971-2.
[45] S.K. Sahoo, S. Biswas, L.S. Toth, P.C. Gautam, B. Beausir, Strain hardening, twinning and texture evolution in magnesium alloy using the all twin variant polycrystal modelling approach, Int. J. Plast. 128 (2020) 1-30, doi:10.1016/j.ijplas.2020.102660.
[46] S.K. Sahoo, L.S. Toth, A. Molinari, M.I. Latypov, O. Bouaziz, Plastic energy-based analytical approach to predict the mechanical response of two-phase materials with application to dual-phase steels, (2021) submitted for publication.
[47] A. Molinari, L.S. Tóth, Tuning a self consistent viscoplastic model by finite element results-I. Modeling, Acta Metall. 42 (1994) 2453-2458, doi:10.1016/0956-7151(94)90324-7.
[48] B. Beausir, J.-J. Fundenberger, Analysis Tools for Electron and X-ray diffraction, ATEX - software, www.atex-software.eu, Université de Lorraine - Metz (2017).
[49] J.D. Seidt, A. Gilat, Plastic deformation of 2024-T351 aluminum plate over a wide range of loading conditions, Int. J. Solids Struct. 50 (2013) 1781-1790, doi:10.1016/j.ijsolstr.2013.02.006.
[50] C. Chen, Y. Beygelzimer, L.S. Toth, Y. Estrin, R. Kulagin, Tensile yield strength of a material preprocessed by simple shear, J. Eng. Mater. Tech. 138 (2016) 031010, doi:10.1115/1.4033071.
[51] A. Orozco-Caballero, F. Li, D. Esqué-de los Ojos, M.D. Atkinson, J. Quinta da Fonseca, On the ductility of alpha titanium: The effect of temperature and deformation mode. Acta Mater. 149 (2018) 1-10, doi:10.1016/j.actamat.2018.02.022.
[52] H. Mecking, U.F. Kocks, C. Hartig, Taylor factors in materials with many deformation modes, Scr. Mater. 35 (1996) 465-471, doi:10.1016/1359-6462(96)00137-6.

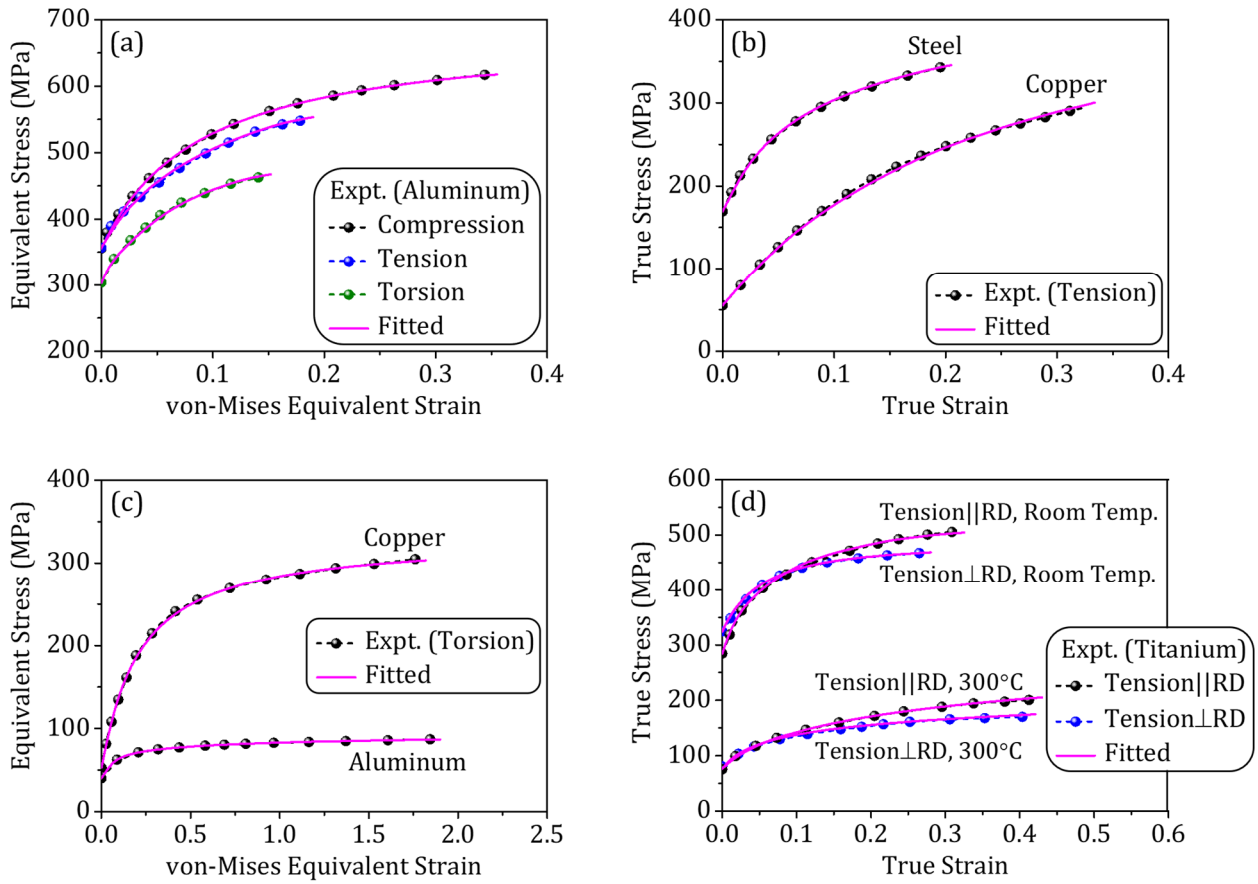

Fig. 1. Fitted stress-strain response obtained from analytical phenomenological hardening curve, compared to measurements.

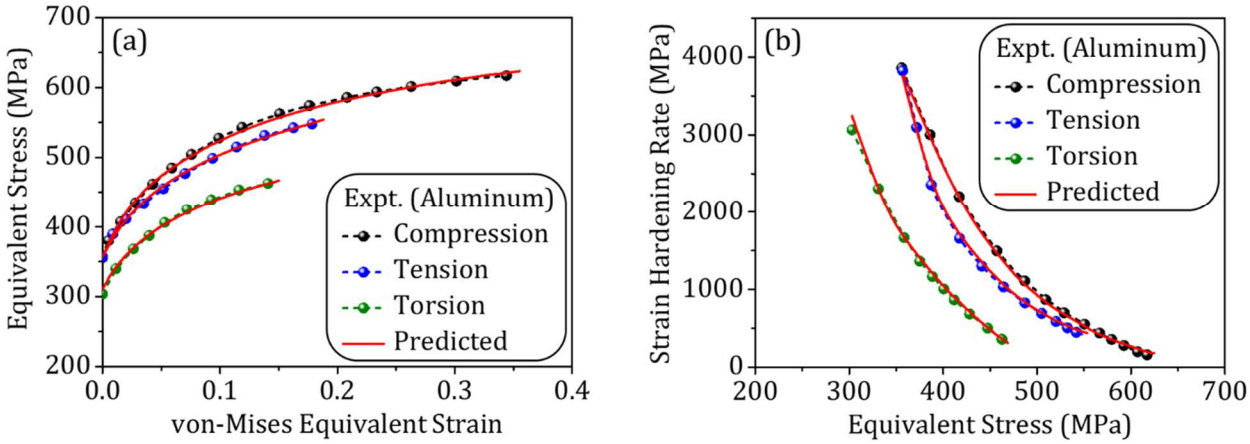

Fig. 2. VPSC simulation results for aluminum (Al 2024) in comparison with experimental measurements for (a) stress-strain response and (b) strain hardening rate.

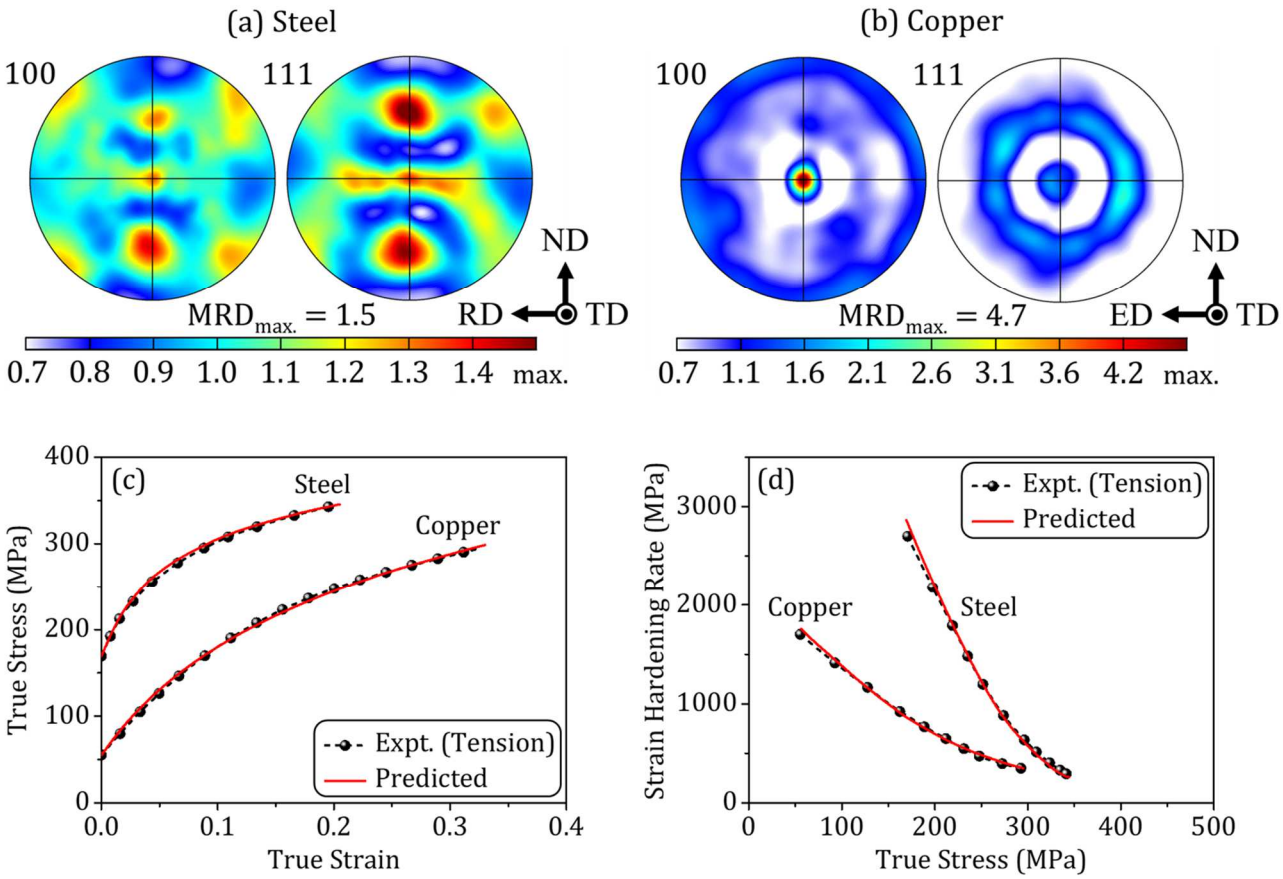

Fig. 3. Initial input texture used for VPSC simulation for (a) Steel and (b) Copper (C110). Comparative plots of both the experimental and predicted (c) stress-strain response and (d) strain hardening rate behavior of both the tested specimens obtained from the VPSC simulation.

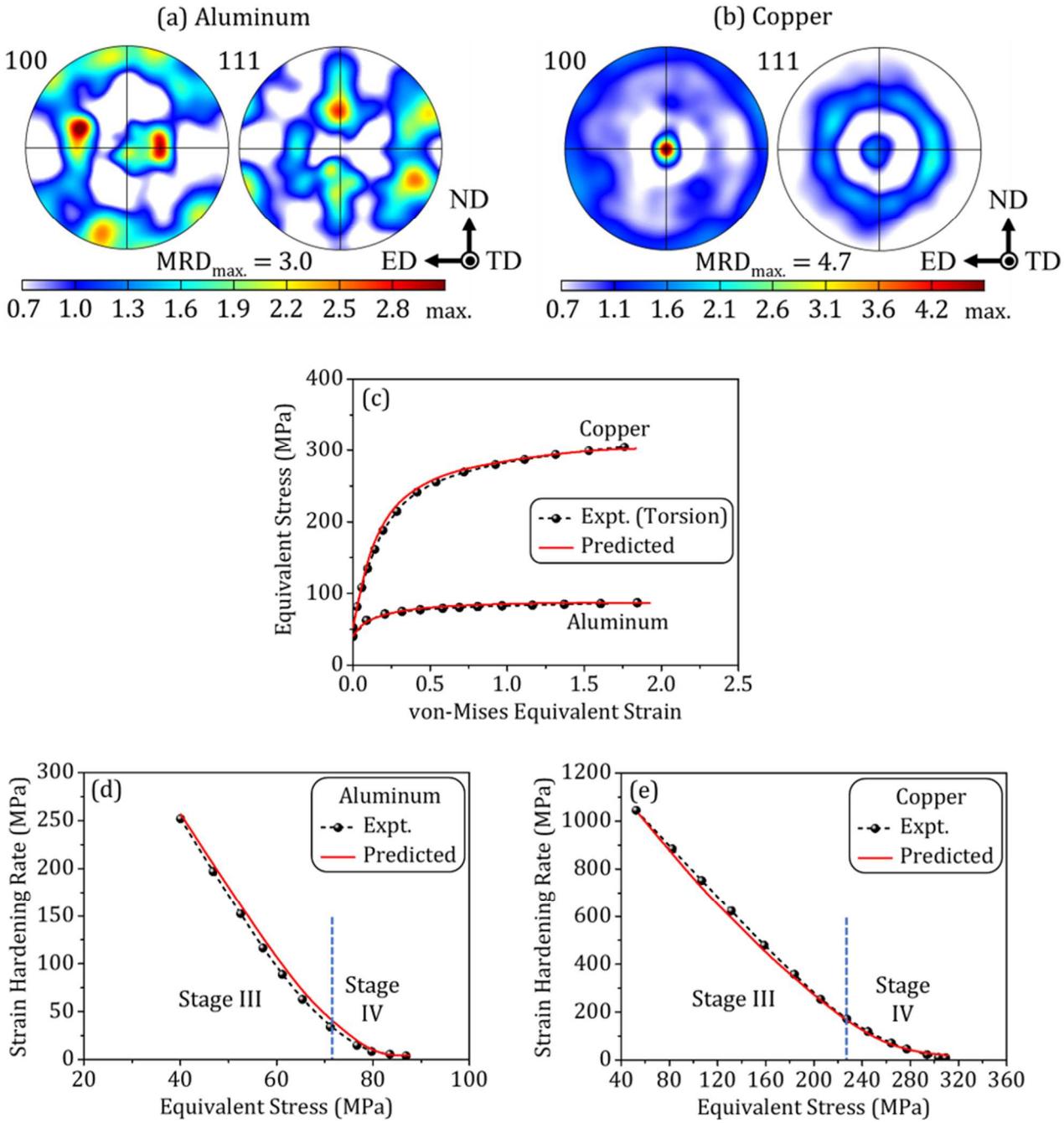

Fig. 4. Initial input texture used for VPSC simulation for (a) Aluminum (Al 1050) and (b) Copper (C110). Comparative plots of both the experimental and predicted (c) stress-strain response and (d-e) strain hardening rate behavior of both the tested specimens obtained from the VPSC simulation.

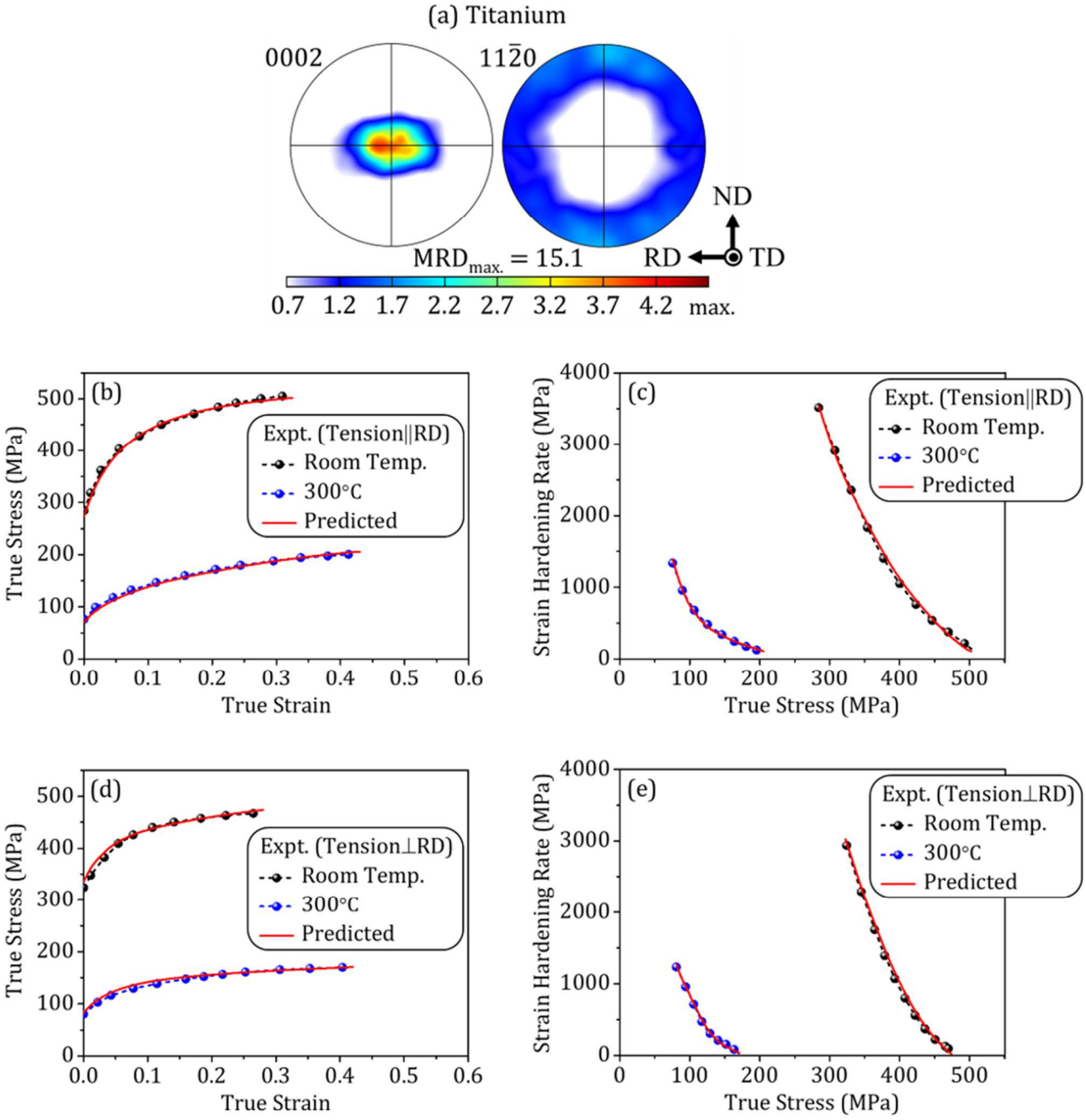

Fig. 5. Initial input texture used for VPSC simulation for (a) rolled titanium (CP-grade 2) sample similar to the published literature (Orozco-Caballero et al., 2018).
(b-e) Comparative plots of both the experimental and predicted stress-strain response and strain hardening rate behavior obtained from the VPSC simulation for tension parallel and perpendicular to the rolling direction at room temperature and 300°C.

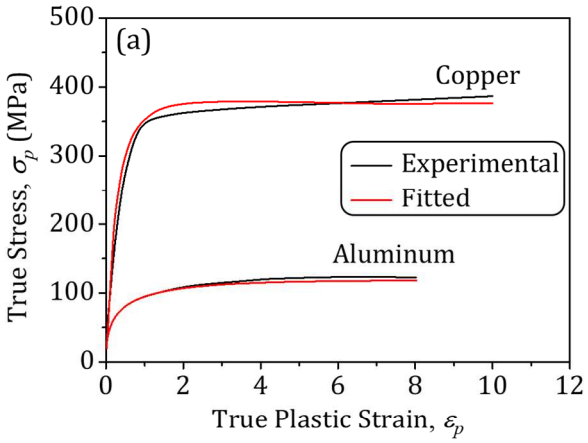

Exponential power-law relationship (Chinh et al., 2004):

$$\sigma = \sigma_0 + \sigma_1\left[1 - exp\left(\frac{-\varepsilon^n}{\varepsilon_c}\right)\right]$$

Parameters used: $\sigma_0, \sigma_1, \varepsilon_c, n$

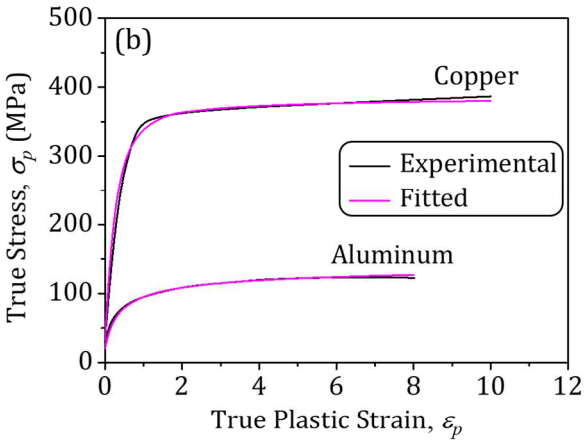

Proposed analytical equation:

$$\sigma_0(\bar{\varepsilon}) = \sigma_{sat} - \sigma_{sat}\left[\left(\frac{h(a-1)}{\sigma_{sat}}\right)\bar{\varepsilon} + \left(1 - \frac{\sigma_{00}}{\sigma_{sat}}\right)^{1-a}\right]^{\frac{1}{1-a}}$$

Parameters used: $\sigma_{00}, \sigma_{sat}, h, a$

Fig. 6. Comparison of the strain hardening plots between (a) the function of Chinh et al. (2004) and (b) the proposed analytical phenomenological function.

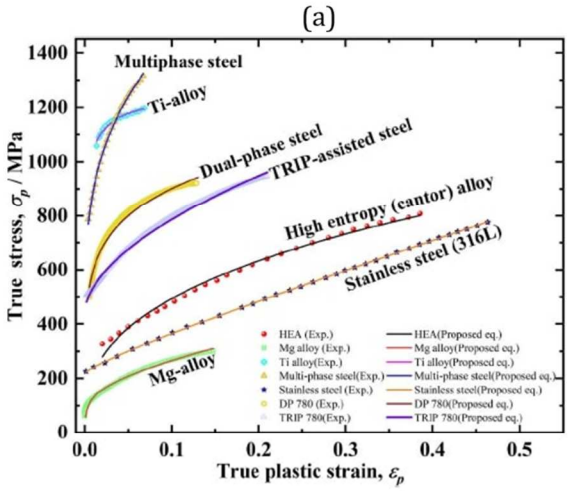

Modified Ludwigson equation (Lavakumar et al., 2021):

$$\sigma = K_1\varepsilon_p^{n_1} + exp(K_2 + n_2\varepsilon_p) - ex\,p(K_3 + n_3\varepsilon_p)$$

Parameters used: $K_1, n_1, K_2, n_2, K_3, n_3$

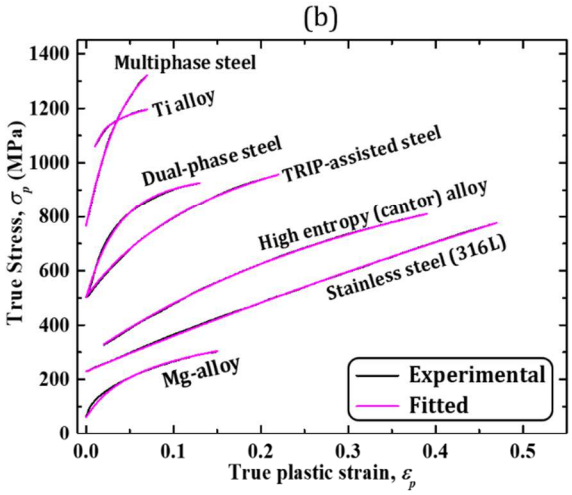

Proposed analytical equation:

$$\sigma_0(\bar{\varepsilon}) = \sigma_{sat} - \sigma_{sat}\left[\left(\frac{h(a-1)}{\sigma_{sat}}\right)\bar{\varepsilon} + \left(1 - \frac{\sigma_{00}}{\sigma_{sat}}\right)^{1-a}\right]^{\frac{1}{1-a}}$$

Parameters used: $\sigma_{00}, \sigma_{sat}, h, a$

Fig. 7. Comparison of the strain hardening plots between (a) the modified Ludwigson function (Lavakumar et al. (2021)), and (b) the proposed analytical phenomenological function.

Table 1. The hardening parameters obtained by fitting the new phenomenological hardening law for different materials and testing conditions.

Figure	Material, Testing	Yield strength (σ_{00}) [MPa]	Saturation stress (σ_{sat}) [MPa]	Hardening coefficient (h) [MPa]	Hardening exponent (a)
Fig. 1a	Aluminium Compression at RT	355	995	30940	4.90
	Aluminium Tension at RT	357	955	31221	4.90
	Aluminium Torsion at RT	300	879	21953	4.90
Fig. 1b	Copper Tension at RT	56	695	2127	3.10
	Low Carbon Steel Tension at RT	170	640	13998	4.89
Fig. 1c	Copper Torsion at RT	52	390	1839	3.10
	Aluminium Torsion at RT	42	98	3268	4.52
Fig. 1d	Titanium Tension ∥ RD, RT	284	528	12578	1.61
	Titanium Tension ⊥ RD, RT	324	485	16317	1.61
	Titanium Tension ∥ RD 300°C	76	390	2350	4.08
	Titanium Tension ⊥ RD 300°C	80	305	2866	4.08

Table 2. The predicted and the adjusted values of the Taylor factor for different materials, the λ parameter and the test conditions obtained by VPSC simulation.

Figure	Material, testing, initial texture	{VPSC} adjusted Taylor factor	λ
Fig. 2	Aluminium Compression at RT Random texture	{2.47} 2.22	1.15
	Aluminium Tension at RT Random texture	{2.49} 2.23	1.14
	Aluminium Torsion at RT Random texture	{2.39} 1.87	1.12
Fig. 3	Copper Tension at RT Measured texture	{2.43} 2.24	1.15
	Low Carbon Steel Tension at RT Measured texture	{2.34} 2.05	1.14
Fig. 4	Copper Torsion at RT Measured texture	{2.41} 2.08	1.13
	Aluminium Torsion at RT Measured texture	{2.42} 2.1	1.11
Fig. 5	Titanium Tension ∥ RD, RT Measured texture	{2.20} 2.59	1.09
	Titanium Tension ⍰ RD, RT Measured texture	{2.26} 2.95	1.2
	Titanium Tension ∥ RD, 300°C Measured texture	{2.25} 2.11	1.06
	Titanium Tension ⍰ RD, 300°C Measured texture	{2.38} 2.22	1.14

Table 3. The hardening parameters used in the VPSC simulations to fit the phenomenological hardening law corresponding to different materials and test conditions.

Figure	Material, testing, initial texture	Taylor Factor	τ_0 for {111}<110> [MPa]	Saturation stress (τ_{sat}) [MPa]	Hardening coefficient (h_c) [MPa]	Hardening exponent (a_c)
Fig. 2	Aluminium Compression at RT Random texture	2.22	160	421	6278	4.90
	Aluminium Tension at RT Random texture	2.23	160	394	6278	4.90
	Aluminium Torsion at RT Random texture	1.87	160	388	6278	4.90
Fig. 3	Copper Tension at RT Measured texture	2.24	25	253	424	3.10
Fig. 4	Copper Torsion at RT Measured texture	2.08	25	190	424	3.10
	Aluminium Torsion at RT Measured texture	2.1	20	43	706	4.52

Table 4. The hardening parameters used in the VPSC simulation to fit the phenomenological hardening law corresponding to steel.

Figure	Material, testing, initial texture	Taylor Factor	τ_0 for {110}<111> [MPa]	τ_0 for {112}<111> [MPa]	Saturation stress (τ_{sat}) [MPa]	Hardening coefficient (h_c) [MPa]	Hardening exponent (a_c)
Fig. 3	Steel Tension at RT Measured texture	2.05	83	79	299	3331	4.89

Table 5. The hardening parameters for HCP-Ti tensile testing used in VPSC simulations.

Figures	Material, testing, initial texture	Saturation stress (τ_{sat}) (MPa)	Hardening coefficient (h_c) (MPa)	Hardening exponent (a_c)
Fig. 5	Titanium Tension ‖ RD, RT Measured texture	317	1875	1.61
	Titanium Tension ⍰ RD, RT Measured texture	286	1875	1.61
	Titanium Tension ‖ RD, 300°C Measured texture	180	528	4.08
	Titanium Tension ⍰ RD, 300°C Measured texture	153	528	4.08

Table 6. Initial Reference Resolved Shear Stresses for hexagonal slip system families, in [MPa].

	Prismatic	Basal	Pyramidal <a>	Pyramidal <c+a>
RT	110	179	142	243
300°C	36	36	36	254